Journal of Micromechanics and Microengineering

PAPER

Hydrodynamic channeling as a controlled flow reversal mechanism for bidirectional AC electroosmotic pumping using glassy carbon microelectrode arrays

IOP Publishing Journal of Micromechanics and Microengineering

J. Micromech. Microeng. **29** (2019) 075007 (14pp) https://doi.org/10.1088/1361-6439/ab1d9f

Hydrodynamic channeling as a controlled flow reversal mechanism for bidirectional AC electroosmotic pumping using glassy carbon microelectrode arrays

Matias Vazquez-Pinon[1], Bidhan Pramanick[2], Felipe G Ortega-Gama[3], Victor H Perez-Gonzalez[1], Lawrence Kulinsky[4], Marc J Madou[1,4], Hyundoo Hwang[5,6] and Sergio O Martinez-Chapa[1,6]

[1] Tecnologico de Monterrey, Escuela de Ingeniería y Ciencias, Ave. Eugenio Garza Sada 2501, Monterrey, N.L., 64849, Mexico
[2] School of Electrical Sciences, Indian Institute of Technology, Goa, Farmagudi, Ponda-403401, India
[3] Department of Physics, College of William and Mary, Williamsburg, VA 23187, United States of America
[4] Department of Mechanical and Aerospace Engineering, University of California, Irvine, 4200 Engineering Gateway, Irvine, CA, United States of America
[5] BBB Inc., 26 Samseong-ro 85-gil, Gangnam-gu, Seoul 06194, Republic of Korea

E-mail: smart@tec.mx and doo@bbbtech.com

Received 7 February 2019, revised 12 April 2019
Accepted for publication 29 April 2019
Published 29 May 2019

Abstract

Controlled bidirectional flow by AC electroosmotic means is achieved using asymmetric coplanar and high-aspect-ratio glassy carbon electrodes and without the involvement of moving elements. The forward and backward fluidic propulsion is the result of hydrodynamic channeling of the fluid in a microfluidic device. The asymmetric coplanar electrodes were fabricated by photolithographic patterning of SU-8 photoresist, followed by pyrolysis at 900 °C. Morphological characterization of the carbon structures was carried out by SEM and confocal microscopy. Then, Raman and EDX spectroscopies confirmed that the resulting carbon material is appropriate for electrokinetic applications. A finite element analysis was carried out to study the flow development by AC electroosmosis. Electrode arrays of three different asymmetry ratios (60 μm:20 μm, 80 μm:20 μm, and 100 μm:20 μm) were fabricated and tested. Fluid velocity was measured for an applied bias in the 2–20 V_{PP} amplitude range, and in the 1 kHz to 200 MHz frequency range. Overall maximum measured forward and reverse fluid velocities were 28.59 μm s^{-1} and 338 μm s^{-1}, respectively. On an additional set of devices with the same asymmetry ratios, a second photolithography step was utilized to produce high-aspect-ratio microposts on top of the coplanar electrodes to study the effect of high electrode contact surface to generate bidirectional flow. Using the same amplitude and frequency ranges as for planar structures in experimental testing, the overall maximum measured velocities were 9.23 μm s^{-1} and 90.66 μm s^{-1} for the forward and reverse regimes, respectively. In contrast to the planar electrodes, microposts-containing electrodes had more balanced velocity magnitudes between reverse and forward flows as the asymmetry ratio increases. In this case, the use of this electrode topology can be useful when symmetry of the forward and backward flow is more important than the magnitude of the volumetric flow rate.

[6] Authors to whom correspondence should be addressed.

Keywords: AC electroosmosis, micropumps, hydrodynamic channeling, carbon-MEMS, bidirectional pumping

S Supplementary material for this article is available online

(Some figures may appear in colour only in the online journal)

1. Introduction

The appropriate microfluid transport mechanism operating in low Reynolds number regimes is fundamental for the optimal performance of chemical/biological analysis systems, such as lab-on-a-chip (LoC) and micro total analysis systems (μTAS). In such systems, fluid transport is typically used for sample distribution in microchannel networks, reagent/sample mixing and biomolecular separations, among many other tasks.

The need for small footprint, portability, and low power consumption of LoC and μTAS systems have motivated the quest for simple and cost-effective on-chip fluid pumping mechanisms. To date, a fairly large selection of micropumps have been developed. They are commonly classified into displacement and dynamic micropumps [1, 2]. Displacement micropumps make use of pressure forces generated by a physical moving actuator on a volume of fluid. These systems include piezoelectric [3], pneumatic [4] and electrostatic [5] micropumps, among others. However, fabrication of these devices often requires complex and expensive micromachining processes, and there is an inherent propensity for mechanical wearing, fatigue, and clogging that might limit the micropump throughput and cause premature failure.

To overcome limitations of displacement mechanisms, pumping techniques with no moving parts have been successfully implemented in microfluidic systems, which are referred to as dynamic micropumps. Here, various types of transmitters continuously transfer non-mechanical energy directly to the fluid to generate momentum. The most extensively studied dynamic approaches include thermal [6], electrohydrodynamic (EHD) [7], magnetohydrodynamic (MHD) [8], and DC and AC electroosmotic micropumps [9, 10]. In this case, the lack of moving parts significantly simplifies the micropump structural framework, generally leading to a straightforward and cost-effective device fabrication process. EHD and DC electroosmosis (DCEO) pumping approaches have been studied extensively; however, the extremely high operational voltages affect the electrical properties of the fluid and require bulky external power generators [11]. Moreover, for MHD pumping the use of external magnets/electromagnets is required [12], which limits the ability to integrate all the elements into a single portable device.

On the other hand, it has been recognized that AC electroosmosis (ACEO) has the advantage of low structural complexity (commonly constituted only by an electrode array). Also, due to its direct and localized actuation, ACEO allows the development of independent fluid control mechanism at different microchannel locations and at different phases of the analysis process [13–17].

In ACEO, a low-amplitude (0–10 V_{PP}), low-frequency (10 Hz–10 kHz) AC signal is applied across electrode pairs separated by a few micrometers gap to induce a strong, non-uniform electric field that propels ions in the fluid adjoining the electrodes [18]. Movement of these ions and their hydrated shells is transferred to the surrounding fluid by viscous forces [19]. In order to cause net flow (and not just re-circulation above the electrodes), asymmetry in electrode geometry is introduced, by having a narrow electrode E_N paired with a wider electrode, E_W. In this work the term *forward flow* indicates the net flow of the fluid from E_N towards E_W (see figure 1).

Even though ACEO is commonly employed as a unidirectional pumping mechanism, in this work we take advantage of the geometry of the microchannel enclosing the fluid to hydrodynamically reverse the net flow direction (i.e. force the net flow from E_W towards E_N). That is, we take advantage of the geometrical characteristics of the microchannel enclosing the fluid to force the flow to reverse by preventing the vortices to complete a swirl in the direction of the forward flow. Therefore, a bidirectional ACEO micropump is developed where the control of the fluid direction is enacted by adjusting the applied AC signal. The bidirectional pumping can be effectively used in LoC systems [20]. For example, bidirectional fluid movement can be used to decrease convective mixing time for sample preparation [21], to increase efficiency in separation and sorting applications [22], to overcome reciprocating centrifugal forces in CD-fluidics [23] and to reduce processing time of DNA hybridization [24]. Additionally, the use of reciprocation (the alternating use of forward and reverse propulsion) can increase the speed of high-affinity bindings in analyte-surface interactions in immunoassays [25] and increase the efficiency label-free electrochemical biosensing [26]. Finally, bidirectional flow can also be utilized to optimize dose control in drug delivery devices [27].

In order to produce ACEO bidirectional pump, a wide electrochemical stability of electrode material is essential to guarantee optimal performance without electrode degradation and bubble formation. The carbon-MEMS (C-MEMS) process have shown to be a potential candidate to fabricate cost-effective glassy carbon (GC) electrodes [28]. In this process, a photolithographically-patterned organic precursor is reduced to GC at 900 °C in an oxygen-free environment [29]. The C-MEMS process for GC electrode fabrication has been successfully implemented for ACEO pumping [30], biosensing [31], energy generation [32] and energy storage [33], among others.

We report on the development of bidirectional ACEO pumping by means of hydrodynamic channeling of fluid

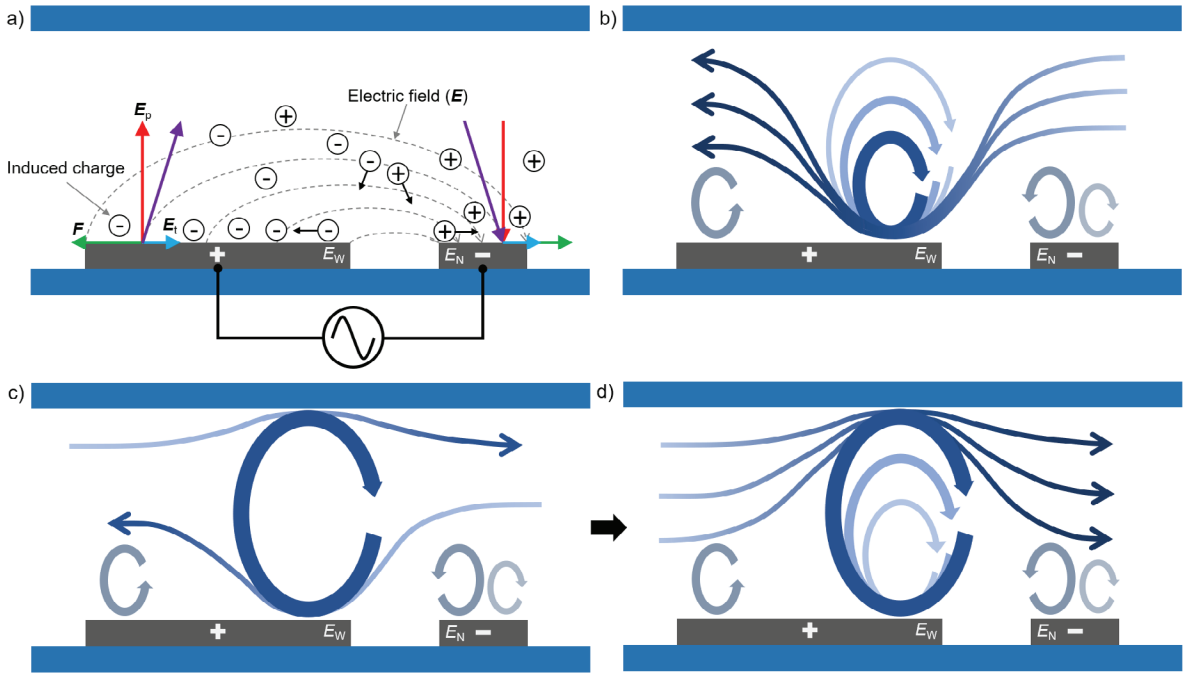

Figure 1. Development of fluid flow by AC electroosmosis with asymmetric coplanar microelectrodes: (a) electric field distribution and induced EDL formation, (b) forward flow generated at the electrodes surface, (c) transition point where flow generated at electrodes' surface is offset completely by development of the reversed flow at the top of the channel, and (d) reverse flow generated at the top of the channel dominating mass transport at high AC amplitudes.

streamlines contained in a microfluidic channel. The geometric relation between asymmetric coplanar electrodes and the microchannel geometry allowed us to drive fluid in both forward and reverse directions by controlling the applied AC signal. Additionally, 3D high-aspect-ratio (HAR) microposts were developed atop the planar electrodes to explore the effect of high-surface-area microstructures on bidirectional flow development. The electrodes were fabricated using the conventional C-MEMS process. The resulting GC material was characterized by Raman and energy-dispersive x-ray (EDX) spectroscopies to confirm that the electrode material properties (composition and graphitic/amorphous carbon content) are appropriate for utilization of these electrodes for electrokinetic applications. A finite element model was developed to show the effect of the induced electric double layer (EDL) at the electrodes surface on the vortex formation in the bulk fluid. Finally, experimental tests were carried out and fluid velocities in reverse and forward directions were computed for three electrode asymmetry ratios for both, coplanar and HAR structures, and the results were analyzed and discussed.

1.1. Bidirectional flow development

Asymmetric-coplanar IDEAs are commonly used to generate ACEO flow in microchannels by capacitive electrode polarization. Figure 1(a) shows the electric field distribution, $\boldsymbol{E}$, when an AC potential is applied across one pair of interdigitated electrodes. Here, the perpendicular component of the electric field, $\boldsymbol{E}_p$, draws neighboring opposite-charge ions suspended in the fluid towards the electrodes surface, establishing an induced EDL; whereas its tangential component, $\boldsymbol{E}_t$, induces a force, $\boldsymbol{F}$, that dispels such charges away from the gap between the electrode pair across the diffuse layer of the EDL. Switching electrode polarization draws opposite charges every half-cycle of the AC signal in the same direction [34]. The ionic displacement caused by the momentum transfer from the electrodes to the neighboring charges, allow the development of vortices above the electrodes by viscous forces exerted on the fluid molecules. These vortices sustain their flow direction even though the polarizing signal alternates from positive to negative or vice versa, since the drawn charges from the bulk fluid also alternate to satisfy electrostatic attraction forces. The size of vortices is proportional to the electrode width; thus, the electrode asymmetry ratio establishes a net flow in the direction from the weak vortex over E_N (narrow electrode), towards the dominant vortex over E_W (wide electrode).

However, the net flow direction is not only electrostatically determined by the polarization of asymmetric electrodes. Hydrodynamically, the microchannel enclosing the fluid plays a critical role for establishing flow reversal when the dominating vortex streamlines reach the top of the channel. In the forward direction (i.e. flowing from E_N towards E_W), the dominating vortex establishes the flow direction by dragging fluid molecules neighboring the electrode surface as presented schematically in figure 1(b). As the size of the dominant vortex increases (with an increase in the AC amplitude), it eventually reaches the top of the microchannel. At this point, a stagnation (or transition) point is reached, where no net flow is observed, as shown in figure 1(c), when the forward flow initiated at the bottom of the fluidic channel is completely offset by the reversed flow at the top of the channel. Further increase in the

dominant vortex size causes flow reversal by affecting larger mass transport at the top of the fluidic channel compared to the smaller (forward) flow at the surface of the electrode E_W, as seen in figure 1(d).

2. Methods

2.1. Electrodes fabrication and characterization

The interdigitated electrode arrays (IDEAs) were fabricated following the conventional C -MEMS process, which comprises photolithographic patterning of an organic carbon precursor, followed by pyrolysis. The photolithographic steps were carried out in a class 1000 cleanroom with an ambient temperature of 22 °C and a relative humidity of 38%. All the structures were fabricated on 4-inch, P-type (boron-doped) silicon wafers with a 500 nm thermally-grown SiO_2 layer (NOEL Technologies, Campbell, CA, USA). Before processing, the wafers were cleaned with acetone, isopropyl alcohol and deionized water, and then dehydrated in a convection oven at 120 °C for 20 min. Photomasks were printed on thin acetate film at a resolution of 25 400 DPI for a minimum feature size of 10 μm (CAD/Art Services, Inc. Bandon, OR, USA).

SU-8 2002 photoresist (PR) (MicroChem, Westborough, MA, USA) was spin-coated on the substrate at 1000 rpm for 30 s to a thickness of 3 μm. After a 2 min soft-bake at 95 °C, the thin PR layer was UV-exposed through the IDEAs photomask at an energy flux of 90 mJ cm^{-2} to trigger crosslinking of the exposed resist, followed by a post-exposure bake at 95 °C for 2 min. The structures were then developed by immersing the patterned substrate in SU-8 developer (MicroChem, Westborough, MA, USA) for 1 min to remove uncrosslinked PR.

To pattern HAR microposts, another layer of resist (SU-8 2050 (MicroChem, Westborough, MA, USA)) was spin-coated directly over the recently-developed planar structures at 1000 rpm for 30 s, to a thickness of 160 μm. The second PR layer was soft-baked at 65 °C for 7 min, and then at 95 °C for 35 min. For the second UV exposure step, the microposts photomask was aligned to the underlying PR electrode structures using a mask aligner (MA56, Süss MicroTec, Garching, DE), and then UV exposed under energy flux of 270 mJ cm^{-2}. Post-exposure baking was carried out at 65 °C for 5 min, and at 95 °C for 13 min. Finally, the HAR structures were developed for 16 min with SU-8 developer (MicroChem, Westborough, MA, USA) on an orbital shaker (3520, Labline Instruments, Maharashtra, IN) at 70 rpm to allow the developer to permeate small gaps between adjacent microposts.

Finally, the patterned structures were pyrolyzed in an open-ended quartz tube furnace (RD-M, R.D. Webb Company, Inc., Natick, MA, USA) to obtain the final carbon electrodes. Once the samples were placed in the tube, a high purity N_2 gas flow was diffused across the tube for 10 min at room temperature at a rate of 2.4 l min^{-1} to remove any oxygen trace—the N_2 flow was kept constant throughout the entire process. The tube temperature was then increased from room temperature to 300 °C at a rate of 5 °C min^{-1} and maintained at 300 °C for 1 h and then ramped up from 300 °C to 900 °C at a rate of 10 °C min^{-1} and maintained at that maximum temperature for 1 h. The furnace was then turned off to allow the samples to passively cool down to room temperature. The N_2 flow was stopped when the tube cooled down to 150 °C. The complete fabrication process, including the 2-step photolithography patterning and pyrolysis is illustrated in figure 2.

A 500 μm-wide, 100 μm-high microchannel was patterned in a PDMS matrix by soft-lithography using a SU-8 positive master. The PDMS stamp, prepared with a 10:1 monomers-to-curing agent ratio mix (Sylgard 184, Dow Corning Corp, Midland, MI, USA), was bonded to the silicon chip containing the carbon IDEAs after the 2 min exposure of the PDMS stamp to room air plasma at 30 W and 150 mTorr.

The fluid propulsion mechanism comprises two pumping chambers containing electrode pairs confined in the PDMS microchannel (see figure 3). Three asymmetry ratios for the wide and narrow electrodes, E_W/E_N, were utilized for the planar electrodes: (i) 60 μm:20 μm, (ii) 80 μm:20 μm, and (iii) 100 μm:20 μm. Furthermore, devices (iv), (v) and (vi) were fabricated by developing 80 μm-height (after pyrolysis) HAR microposts on top of a separate set of planar electrodes with the same asymmetry ratios as those of (i), (ii) and (iii), respectively. In all cases, the inner gap (i.e. the distance between opposite electrodes of the same pair) is $G_1 = 20$ μm, and the outer gap (i.e. distance between consecutive electrode pairs) is $G_2 = 100$ μm. The total length of each pumping chamber is 6 mm, thus containing 30, 27 and 25 electrode pairs for devices (i) and (iv), (ii) and (v), and (iii) and (vi), respectively. Electrode fingers are 3.6 mm long, and each electrode pair switches widths ($E_W \leftrightarrow E_N$) halfway from base to the outer end of the finger, while preserving inner and outer gap lengths, as shown in the inset of figure 3. The flow direction is split into forward and reverse regimes, determined by the direction of the net flow with respect to the electrode arrangement: forward for a flow going from E_N, through G_1, toward E_W; and reverse for a flow in the opposite direction [35, 36], as depicted in the inset of figure 3.

Thickness and volumetric shrinkage of the resulting carbon structures were characterized using confocal microscopy (Axio CSM 700, Carl Zeiss AG, Oberkochen, DE). Physical inspection and imaging of microstructures were carried out by scanning electron microscopy (SEM) (EVO MA25, Carl Zeiss AG, Oberkochen, DE). Elemental composition of the pyrolyzed material was determined by Energy Dispersive Spectroscopy (EDS) (XFlash 6|10, Bruker Corp., Billerica, MA, USA). The electrochemical properties of the pyrolyzed carbon depend upon the type of carbon precursor and the pyrolysis conditions. Raman spectroscopy (inVia Raman microscope, Renishaw, UK with 514 nm Argon laser, Modu-Laser, LLC, Centerville, UT, USA) was used to determine the graphitic (sp^2) and amorphous carbon (sp^3) crystallites content of the electrodes.

A testing solution of distilled water (with a conductivity of $\sigma_f = 5.5$ μS cm^{-1}) containing 1 μm-diameter latex tracers was prepared for experiments. The tracer's size was determined not only considering a favorable visibility under a microscope with a 10× objective, but also to avoid dielectrophoretic effect that might disturb the particle's

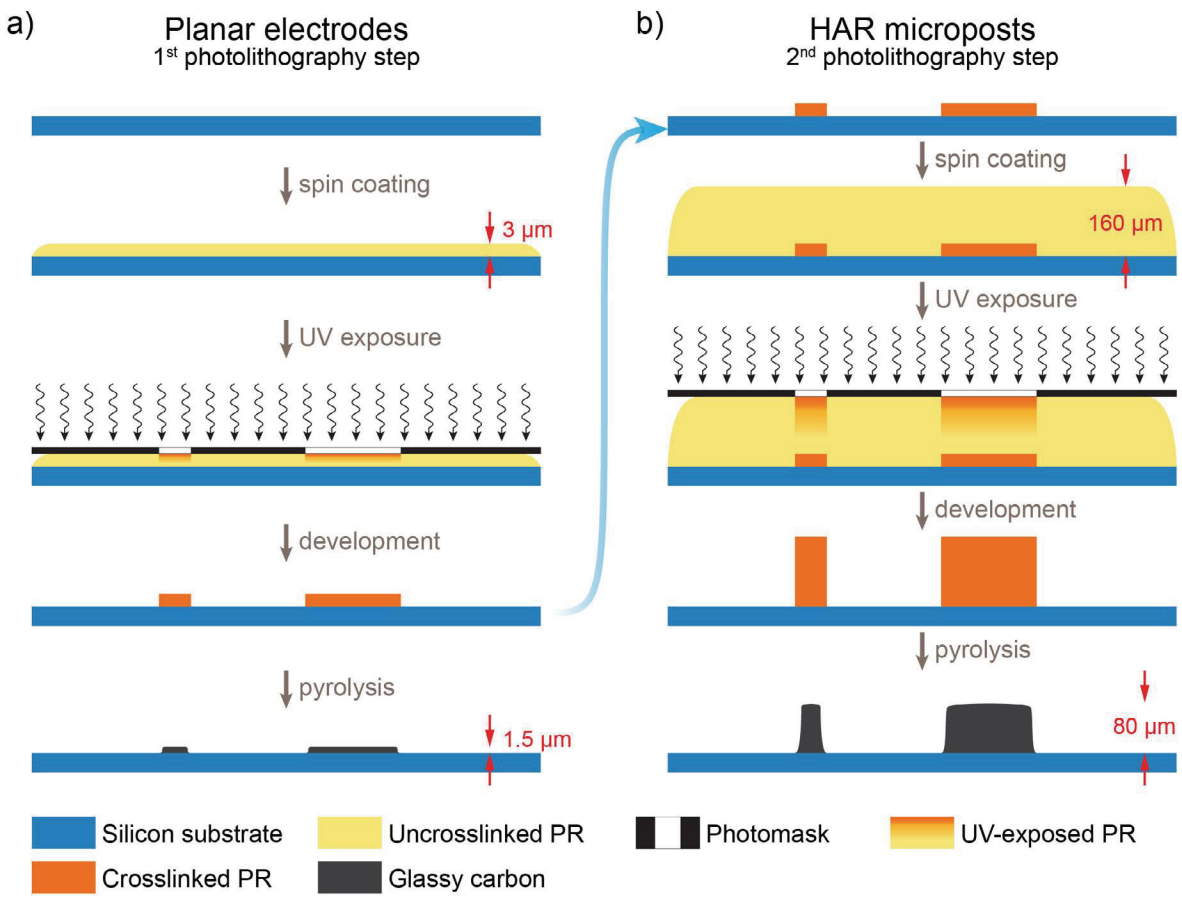

Figure 2. Carbon microelectrode fabrication process: (a) asymmetric coplanar electrodes, and (b) HAR microposts on top of the planar electrodes.

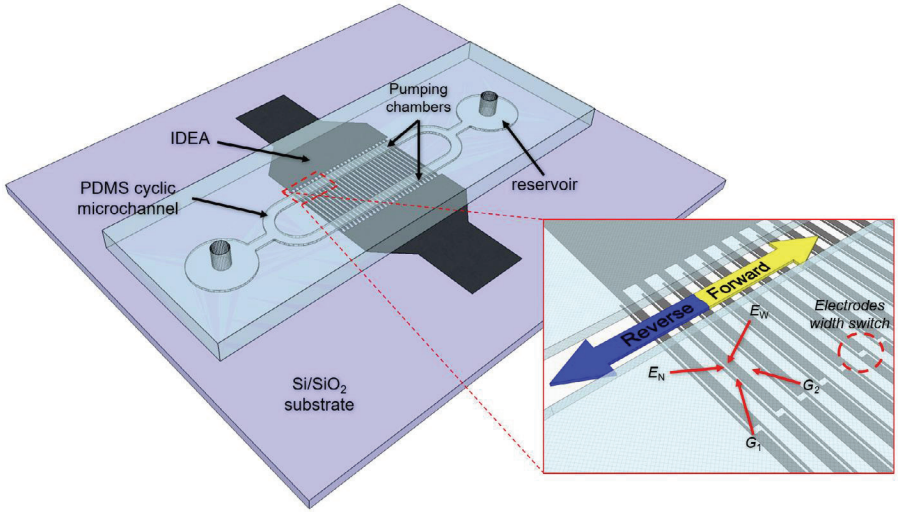

Figure 3. Schematic diagram of the assembled microfluidic chip. The GC IDEA is patterned on the silicon substrate, and the fluid is driven inside the cyclic microchannel by two pumping chambers. The inset shows one pumping chamber and forward flow from E_N through G_2 to E_W, and the reverse flow going in the opposite direction; the electrode width switch is also shown halfway from electrode base to tip for both combs.

velocity on the proximity to the electrodes' surface. All microfluidic devices were degassed for 15 min, and the testing solution was immediately pipetted into the fluidic chambers to avoid bubbles in the microchannels. The electrodes were powered by a sinewave generator (33210A, Agilent Technologies, Santa Clara, CA, USA), while an oscilloscope (TDS 2014B, Tektronix Inc., Beaverton, OR, USA) was used for signal monitoring. Experiments were carried out at the following working frequencies, f_w: 1 kHz, 2 kHz, 10 kHz, 20 kHz, 100 kHz, 200 kHz and 1 MHz.

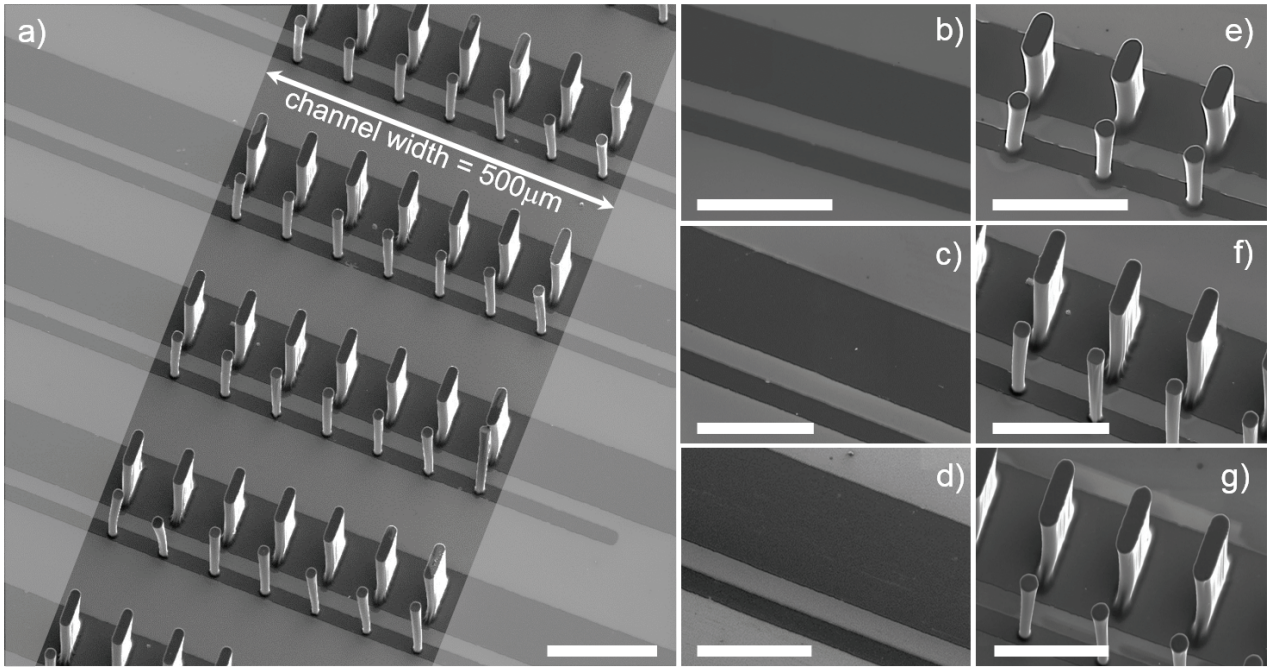

Figure 4. Scanning electron micrographs of the fabricated GC asymmetric coplanar electrodes and HAR microposts. (a) Asymmetric coplanar electrodes with HAR microposts. Coplanar and coplanar with HAR microposts asymmetry ratios, respectively: (b) and (e) 60 μm:20 μm, (c) and (f) 80 μm:20 μm and ((d) and (g)) 100 μm:20 μm. Scale bars = 100 μm.

For each frequency, the signal amplitude was swept from 2 to 20 V_{PP} in 2 V_{PP} steps. The operation of the devices was monitored by an optical microscope (PS-888, Seiwa Optical, Tokyo, JP) with an attached camera (Motic 3000, Motic Instruments, Xiamen, CN) to record 30 s long video clips for each test condition once the flow was fully developed. The fluid velocity was then measured by tracking ten tracers throughout different video frames using a particle tracking software (ImageJ, National Institutes of Health, Bethesda, MD, USA), to later compute their average velocity.

2.2. Finite element analysis

A 2D finite element analysis was carried out using COMSOL Multiphysics (COMSOL, Inc., Stockholm, SE) to analyze the transient flow evolution and the vortex formation during AC electroosmosis. A model that included the periodic section of the coplanar electrode array with an asymmetry ratio of 60 μm:20 μm was used to study the forward mass transport in the system. Flow reversal was not considered in this model. Furthermore, electrothermal effects were also neglected since these are usually relevant at higher working frequencies and larger fluid conductivities. The numerical model utilizes the Poisson equation to find the electric field distribution across a pair of opposite electrodes, $\boldsymbol{E}$; the Nernst–Plank equation is used to determine the charge concentration at the electrodes surface as function of $\boldsymbol{E}$; and the Navier–Stokes equation is employed to establish the fluid velocity and pressure distributions in the system [15]. The electric field across the bulk fluid is given by

$$\mathbf{E} = -\nabla\varphi \tag{1}$$

where φ is the potential difference across the electrode pair. The Poisson equation relates E and the volumetric charge density across the electrolyte:

$$\nabla \cdot (-\varepsilon\nabla\varphi) = \rho_e. \tag{2}$$

Here, $\varepsilon = \varepsilon_0\varepsilon_r$ is the relative permittivity of the medium where ε_0 is the permittivity of vacuum and ε_r is the dielectric constant of the medium. For a symmetric electrolyte (1:1), the electric charge density is given by

$$\rho_e = F\left(c^+ - c^-\right) \tag{3}$$

where $F = 9.6485 \times 10^4$ C mol^{-1} is the Faraday's constant, and c^+ and c^- are the positive and negative ionic concentrations in the fluid, respectively, which are determined by the molar balances:

$$\frac{\partial c_i}{\partial t} = -\nabla \cdot \mathbf{J}_i. \tag{4}$$

Subscript i represents either of the two species; $\mathbf{u}$ is the velocity field, and $\mathbf{J}_i$ is the ionic flux for the ith species. The Nernst–Plank equation gives the ionic flux:

$$\mathbf{J}_i = \boldsymbol{u}c_i - D_i\nabla c_i - \frac{z_i D_i F c_i}{RT}\nabla\varphi \tag{5}$$

where D_i is the diffusion coefficient and z_i is the ion valence of each species; R is the gas constant and T is the fluid temperature. Finally, the velocity and pressure fields for an incompressible, Newtonian fluid across the fluid are described by the Navier–Stokes equation:

$$\rho\left(\frac{\partial \mathbf{u}}{\partial t} + (\boldsymbol{u}\cdot\nabla)\,\mathbf{u}\right) = -\nabla p + \mu\nabla^2\mathbf{u} + \rho_e\nabla\varphi \tag{6}$$

$$\nabla \cdot \mathbf{u} = 0 \tag{7}$$

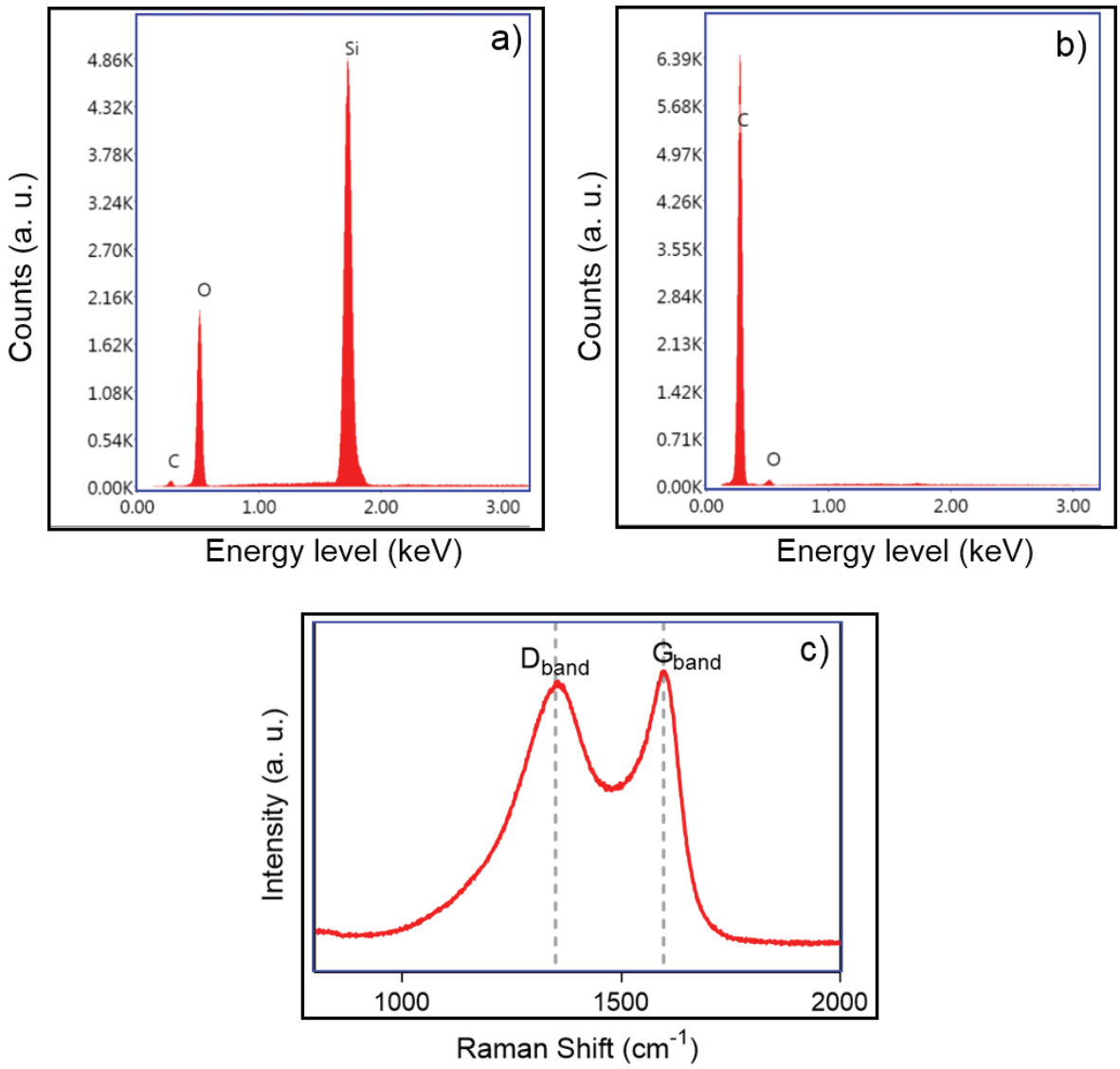

Figure 5. EDX and Raman spectrums of pyrolyzed carbon structures for: (a) planar electrodes; (b) HAR microposts. Si and O peaks shown on plot (a) resulted the SiO_2 film probed due to penetration depth of the EDX electron beam (~20 μm), and (c) Raman spectra of the carbon electrodes fabricated by pyrolyzing SU-8 2002 photoresist at 900 °C for 1 h.

where ρ, p and μ are the density, pressure and the dynamic viscosity of the fluid, respectively.

The model considers one pair of opposite electrodes with the electrodes' widths of $E_N = 20$ μm and $E_W = 60$ μm, a gap between the electrodes $g = 100$ μm, and a microchannel height $h = 100$ μm. A mesh with a total of 16 760 elements was created using an element size of 25 nm at the electrode surface and increasing with the distance from this boundary. All the parameters considered and the boundary conditions are included in the supplementary information (stacks.iop.org/JMM/29/075007/mmedia).

3. Results and discussion

3.1. Electrode characterization

During pyrolysis of the polymeric precursor, non-carbon elements in the material's molecular structure are sublimated, while the remaining carbon atoms are reconstituted, forming sp^2 and sp^3 carbon [37]. Carbonization leads to isometric shrinkage and considerable increase of electrical conductivity of the pyrolyzed material. Figure 4 shows SEM micrographs of the coplanar and HAR microelectrodes of different asymmetry ratios after pyrolysis.

Before pyrolysis, the height of the coplanar and HAR structures averaged 2.98 μm and 159.74 μm, respectively. Average heights after pyrolysis are 1.28 μm and 75.09 μm for coplanar and HAR structures, respectively, corresponding to a total vertical shrinkage of 57% and 53%. Besides pyrolysis conditions, overall shrinkage strongly relates to pre-pyrolysis geometry of the structures. For instance, for coplanar electrodes, a larger vertical shrinkage is attained for the narrower geometry: 58% for device (i), 56% for device (ii) and 53% for device (iii) (i.e. shrinkage % decreases as the electrode broadens) suggesting an increasing lateral stress caused by the combination of high temperature and strong adhesion of the pyrolyzed structure to the substrate. This effect is yet more evident for the case of HAR microposts, where the structures have a small base area

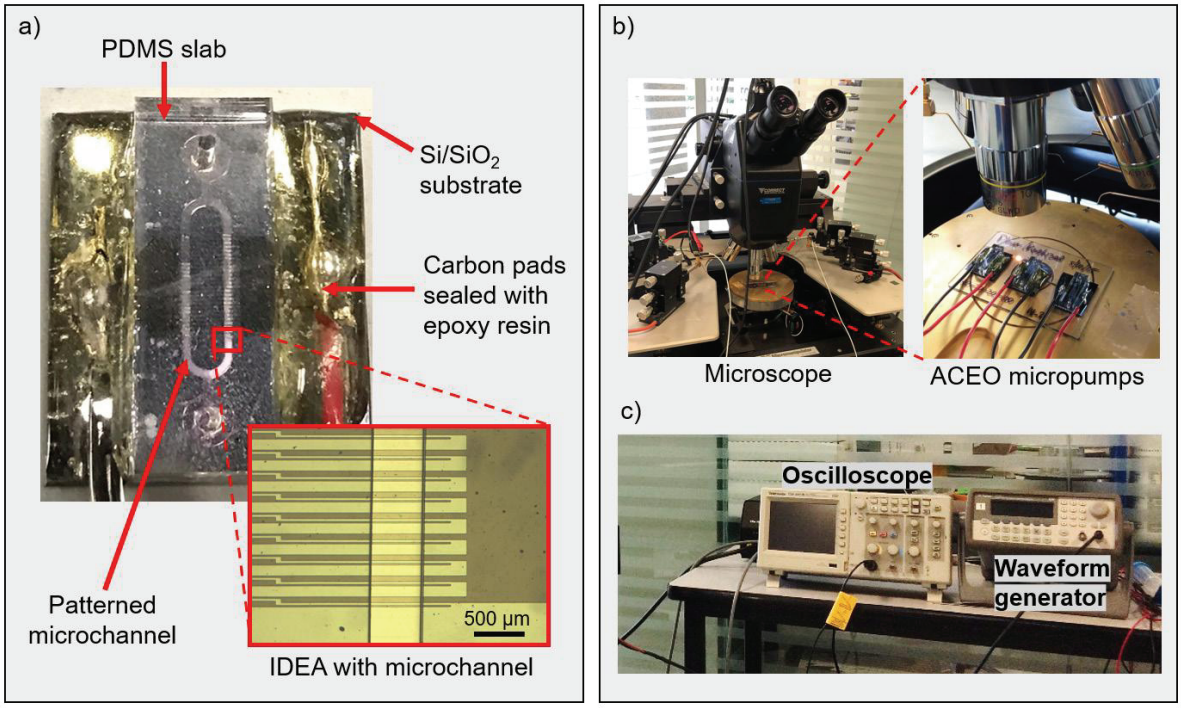

Figure 6. Experimental setup of AC electroosmotic micropumps. (a) Fabricated device, showing PDMS cyclic microfluidic channel and connection pads. Inset shows the microchannel and asymmetric electrode pairs. (b) Microscope, oscilloscope and waveform generator employed for experimental testing.

compared to their vertical dimensions, thus lateral and vertical shrinkages contribute considerably to the volume reduction, averaging 77%, 83%, and 78% for devices (iv), (v) and (vi), respectively. Other parameters, such as temperature and gas pressure fluctuations inside gas furnace can also affect the shrinkage variations.

Elemental composition obtained from EDX analysis of the pyrolyzed structures are shown in figures 5(a) and (b) for both, coplanar and HAR structures, respectively. Planar electrode samples' composition analysis indicates presence of Carbon (55.13 atomic %), Silicon (18.45 atomic %) and Oxygen (26.42 atomic %). The last two elements are the components of the SiO_2 film on the substrate underneath and around the electrodes and probing of the silicon dioxide was due to the penetration depth of the electron beam used for the measurements. No other elements were found in the pyrolyzed material.

EDX spectrum for the HAR structures, in turn, shows a prevailing presence of Carbon (96.02 atomic %), whereas oxygen content is considerably minor (3.98 atomic %) and Silicon is absent. These results are due to the fact that the electron beam was located on top of the micropost, thus reducing the electron beam interaction with the substrate.

Figure 5(c) shows the Raman spectrum of the pyrolyzed carbon material. D- and G-bands, typically seen in GC, were found at 1355 cm^{-1} and 1597 cm^{-1}, respectively. The D-band indicates the presence of sp^3 amorphous carbon structures, while the G-band is characteristic of sp^2 carbon networks forming graphitic nano-crystallites. The G-band for single crystal graphite is usually found at 1575 cm^{-1}, and the band shift is caused by an extremely small crystallite size present in the structure [38]. The intensity ratio of the D-band to the G-band (I_D/I_G) defines the degree of structural disorder with respect to a perfect graphitic crystallite, and consequently, the crystallite size is inversely proportional to this ratio: $1/L_a \propto I_D/I_G$. The I_D/I_G ratio of the pyrolyzed carbon in this work measured 0.96, indicating that the carbon structure is formed by equivalent amounts of ordered (sp^2) and disordered (sp^3) carbon [39]. From EDX and Raman results, it can be concluded that the carbonaceous material conforming the electrodes is GC, which is widely used as electrode material for electrokinetic applications [28].

The device assembled for experimental testing, and the setup used to run and monitor the experiments are demonstrated in figure 6. The inset of figure 6(a) shows a section of the microchannel with the microelectrodes positioned at the bottom of the channel. Figures 6(b) and (c) show the microscope with the attached digital camera and the general-purpose oscilloscope and waveform generator used is the experiments, respectively. Six different devices were tested and collected data include 60 videos for each tested device. This allowed to thoroughly characterize the fluid velocity performance over a wide frequency and amplitude range for three different electrode asymmetry ratios using both planar electrodes and planar electrode system with integrated HAR micropost structures.

3.2. Computational modeling

The fluid velocity development was analyzed for four different frequencies (1 kHz, 10 kHz, 100 kHz, and 1 MHz) at 2 V_{PP} to observe the transient velocity evolution and its

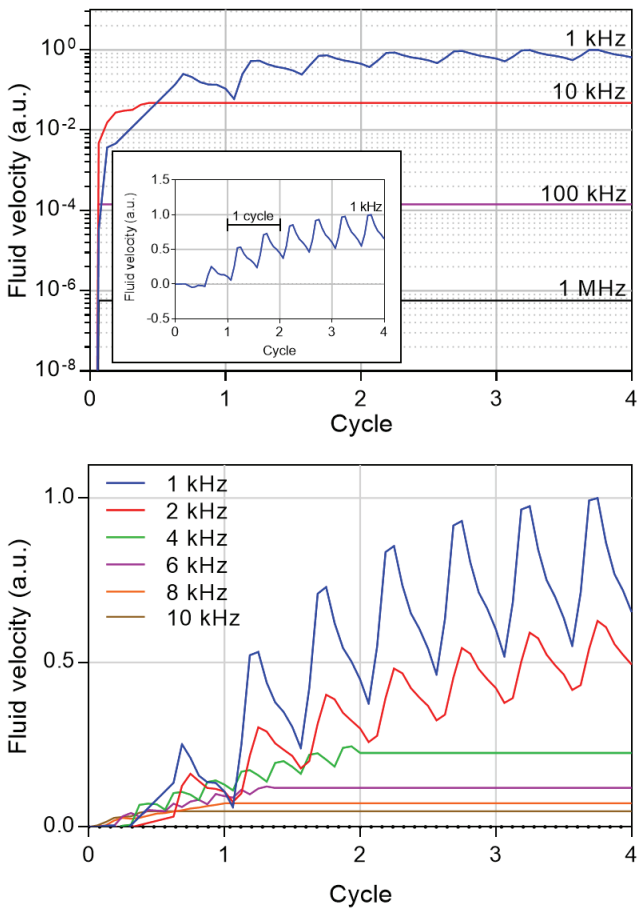

Figure 7. Fluid velocity simulation results: (a) normalized fluid velocity for four AC frequencies at 1 V_{PP}: 1 kHz, 10 kHz, 100 kHz and 1 MHz. Inset shows net fluid velocity evolution of the 1 kHz AC signal in a linear y-axis scale. And (b) normalized fluid velocity for frequencies from 1 kHz to 10 kHz. Fluid velocities are shown as arbitrary units (a.u.).

frequency dependence for a wide frequency range. The net flow evolution, from rest to the first four signal cycles, can be observed in the normalized plot on figure 7(a). The model suggests that for a fixed asymmetry ratio (60 μm:20 μm), 1 kHz signal achieves one order of magnitude higher velocities that the 10 kHz signal, while for higher frequencies (100 kHz and 1 MHz), the net flow becomes negligible. A fast flow development can also be noticed, where the flow is fully developed after four cycles for every case. The pulsating nature of the flow (as easily seen from the inset in figure 7(a)) follows the magnitude of the induced electric field as the AC amplitude evolves through time. Furthermore, the net fluid velocity development for frequencies from 1 to 10 kHz, as plotted in figure 7(b), confirms an exponential velocity decay, even at small frequency steps.

The sequence of images in figure 8 shows the evolution of the vortices (numbered from 1 to 4 from left to right) once the net flow is fully developed in the forward direction (fourth cycle from figure 7 for 1 kHz) throughout half a cycle of the applied signal. Even though the vortices direction is sustained in an alternating electrode polarization, figures 8(a) and (b) show a slight velocity decrease as the AC magnitude increases (this effect is also visible as a small notch in the fluid velocity plot for 1 kHz in figure 7). This is likely caused by charge reordering at electrodes surface as the polarizing signal switches, since co-ions are dispelled, and counter-ions are attracted to form an EDL to satisfy electrostatic equilibrium. As the maximum AC amplitude is reached, vortex 3 becomes dominant over vortices 1, 2 and 4, thus strongly establishing a net flow at this point (figure 8(c)). Finally, all four vortices lose strength as the AC magnitude decreases to complete a cycle (figures 8(d) and (e)).

3.3. Bidirectional pumping

During each half period of the AC signal, $1/(2f_w)$, opposite electrodes alternate their superficial charge, either from positive to negative or vice versa, in response to the oscillation of the applied polarizing signal. At low frequencies, the electrode polarization frequency is close to the characteristic double-layer relaxation frequency, given by $f_{RC} = (1+\delta)\sigma_f\lambda_D/2\pi\varepsilon_f d = 828$ Hz, where δ is the surface capacitance ratio, σ_f is the fluid conductivity, λ_D is the Debye length, ε_f is the fluid permittivity and d is the characteristic macroscopic length scale of the system [40–42] (please refer to table SI3 in the supplementary information for parameters values). In this case, the adjoining suspended ions interact with the polarized electrode, allowing vortex formation to propel the bulk fluid from the EDL. As the working frequency becomes $f_w \gg f_{RC}$, no electrostatic interactions occur due to an extremely short polarization time, thus vortex formation is completely inhibited. Additionally, all devices showed higher fluid velocities for frequencies below 1 kHz at low amplitudes ($<$10 V_{PP}), compared to flows observed at 1 kHz at the same amplitudes, which is in good concordance to the relaxation frequency; however, electrolysis and bubble formation was observed for amplitudes above 10 V_{PP}, leading to electrode degradation.

The fluid velocity was determined using tracers moving across an electrode-free area of the microchannel, having a reasonable distance to the pumping chambers ($>$100 μm). In this sense, it was considered that dielectrophoretic effects on the tracers are negligible, thus their movement solely depends on ACEO flow [15].

Flow direction determined by the movement of the tracers is shown in the sequence of images presented in figure 9. Here, an electrode asymmetry ratio of 80 μm:20 μm was used and E_N is shown as a reference to indicate forward flow from top to bottom of each frame. A 1 kHz AC signal was applied by sweeping the amplitude from 2 to 20 V_{PP}. In figure 9(a) through (c), three tracers are tracked moving towards E_N, while others are static due to fouling and adhesion to the substrate. In this experiment, the forward flow is evident from 10 to 14.4 V_{PP}. Then, at 14.6 V_{PP}, tracers' recirculation without net flow can be observed on figure 9(d) through (f). Here, tracers 1, 2 and 3, are the farthest from the electrodes and have no participation in the formed vortices, but show only Brownian motion; however, tracers 4 and 5, which are closer to the electrodes move towards the electrode surface. At this

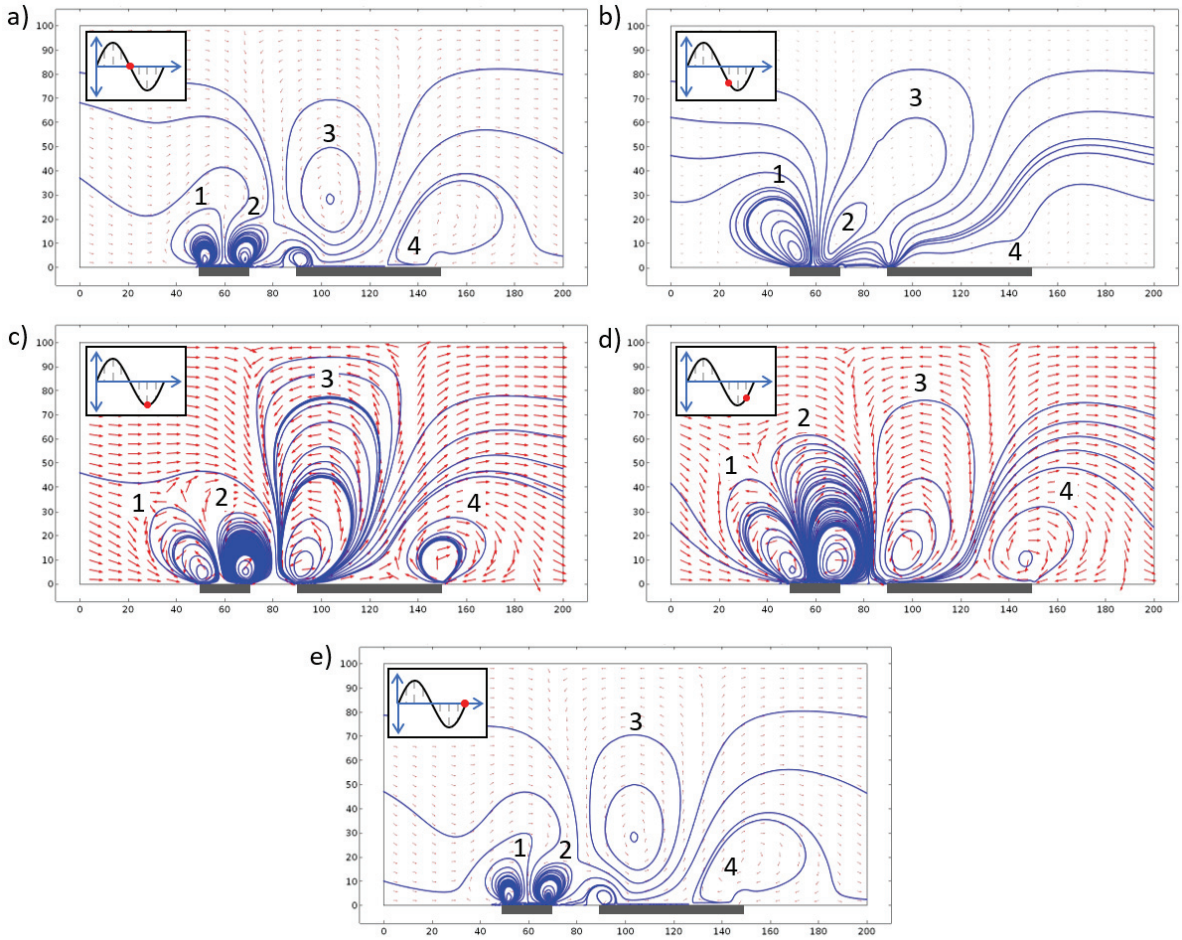

Figure 8. Finite element analysis of vortex formation along the second half of the fourth cycle of the applied AC signal at 1 kHz (fully developed flow): (a) 3.5 ms, (b) 3.625 ms, (c) 3.75 ms, (d) 3.875 ms, and (e) 4 ms. Insets show the AC cycle step. Arrows' lengths indicate the velocity magnitude and direction, whereas the streamlines depict the vortex shape.

point, forward flow at the electrode surface and reverse flow at the top of the microchannel cancel out each other, thus no net flow is produced.

Finally, tracers moving away from the electrode were tracked for signal amplitudes higher than 14.6 V_{PP}, as shown in figure 9(g) through (i). All these effects can be observed yet more clearly on the video included as supplementary information of this report.

The maximum experimental fluid velocities achieved in forward and reverse regimes, respectively, for the asymmetry ratios (i), (ii) and (iii), over the tested working frequency range (1 kHz $\leqslant f_w \leqslant$ 1 MHz) are shown in figures 10(a) and (b). Clearly, the highest forward (figure 10(a)) and reverse (figure 10(b)) velocities are achieved for the lowest working frequencies (1–2 kHz) due to an electrode polarization time larger than the charge relaxation time, and velocities decrease sharply as f_w is increased. For a given device, velocity decreases as frequency increases for both flow regimes due to the lack of charge interaction between suspended ions and polarized electrode surface. This effect was consistently observed on the three different devices for both forward and reverse flows, as can be seen from figures 10(a) and (b), respectively. The velocity ratio of maximum reverse flow to maximum forward flow for devices (i), (ii) and (iii) was 11.82, 11.76 and 13.90, respectively, indicating that fluid velocity difference between reverse and forward fluid movement remains relatively constant, independently of the electrode asymmetry ratio.

The effect of electrode asymmetry ratio on fluid velocity is also visible in figures 10(a) and (b), showing that for the tested devices, the lower the asymmetry ratio, the higher the fluid velocities that can be reached. This suggests that as E_W is increased, more time is required to create uniform charge distribution on the entire electrode surface, since the electric field is stronger across G_1 than across G_2 because opposite electrodes are closer together. This increases the effective separation between adjacent electrode pairs, hence reducing the driving forces on the bulk fluid due to weak vortex interactions.

Figure 10(c) shows the normalized fluid velocity evolution for the electrode systems with three asymmetry ratios in an amplitude range of 0–20 V_{PP} at 1 kHz. Low applied amplitudes (2–8 V_{PP}) produce an undefined velocity pattern due to undeveloped flow. However, at 10 V_{PP} a velocity pattern is established and at 12 V_{PP} the maximum forward flow regime is reached. The fluid velocity is reduced as the asymmetry ratio increases. The highlighted zone shows the transition from forward to reverse regime as the signal amplitude is increased.

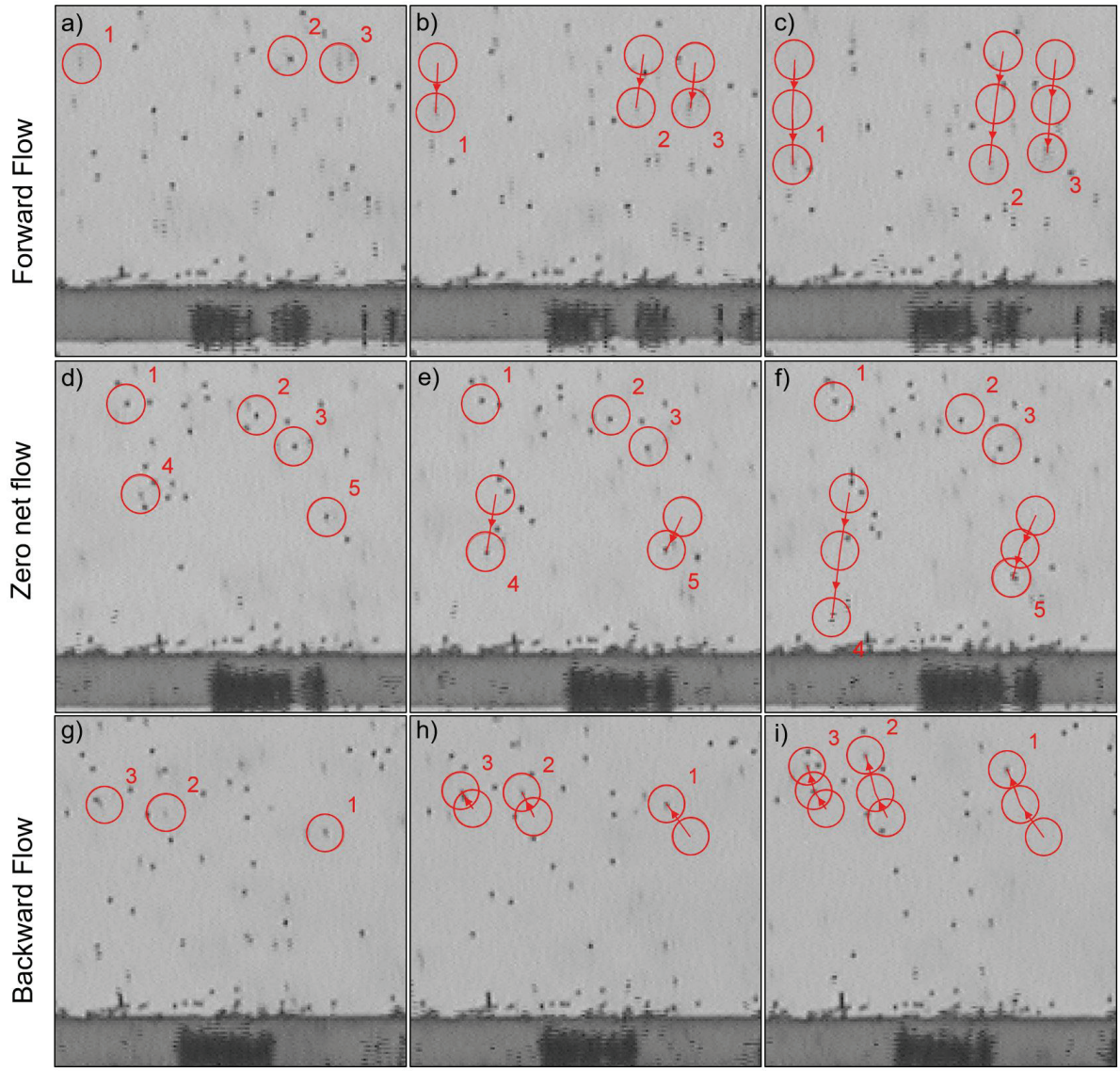

Figure 9. Sequential pictures of tracers tracking during three micropump operational stages: (a)–(c) forward flow; (d)–(f) recirculation of tracers with zero net flow; and (g)–(i) reverse flow. Electrode E_N is shown in all pictures, indicating forward flow as tracers moving from top to bottom of the frame.

This transition occurs between 14 and 16 V_{PP} for the smaller asymmetry ratio (60 μm:20 μm) and between 12 and 14 V_{PP} for larger asymmetry ratios. The same velocity pattern with respect to the asymmetry ratio is observed for the reverse flow as well.

3.4. Effect of microposts on bidirectional flow

Fluid velocity for all the tested devices is mapped in figure 11, including velocity measurements for planar electrodes (figures 11(a)–(c) for devices (i), (ii) and (iii), respectively), and planar electrodes with HAR microposts (figures 11(d)–(f) for devices (iv), (v) and (vi)). Red and blue colors depict areas of forward and reverse regimes, respectively. Hue intensity indicates the relative magnitude of the velocity. Additionally, a demonstration video is available in the supplementary information to illustrate the movement of tracers in the reverse direction when HAR microposts are used to generate ACEO flow.

In contrast to planar electrodes, HAR electrodes (lower row) showed a wider forward flow regime along AC magnitude and frequency, caused by hydrodynamic channeling; however, maximum velocities are lower than for devices with planar electrodes (without posts). Maximum velocities achieved by devices (iv), (v) and (vi) were, respectively, 6.34 μm s^{-1}, 9.23 μm s^{-1} and 6.02 μm s^{-1} in the forward regime; and 79.71 μm s^{-1}, 90.66 μm s^{-1} and 14.66 μm s^{-1} in the reverse regime. These velocities indicate that a higher electrode contact surface with the fluid does not necessarily guarantee a fluid velocity increase. One possible explanation is that closely-spaced posts create a significant drag that retards the propulsion of the flow. Another possibility is that vertically-generated vortices on two facing micropost surfaces

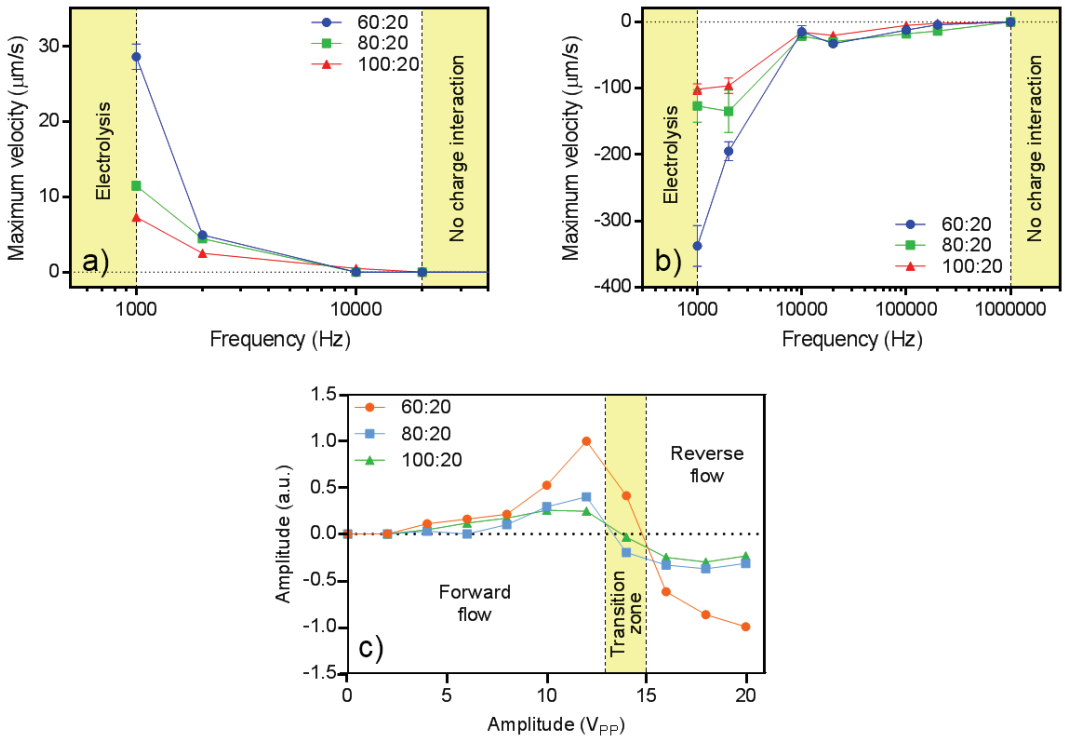

Figure 10. (a) Forward and (b) reverse flow velocity measurements for devices (i), (ii) and (iii), and (c) normalized fluid velocity evolution for the three tested electrode asymmetry ratios. Forward and reverse flows at 1 kHz and amplitudes from 0 to 20 V_{PP}. Highlighted area shows transition from forward to reverse flow as the signal amplitude increases.

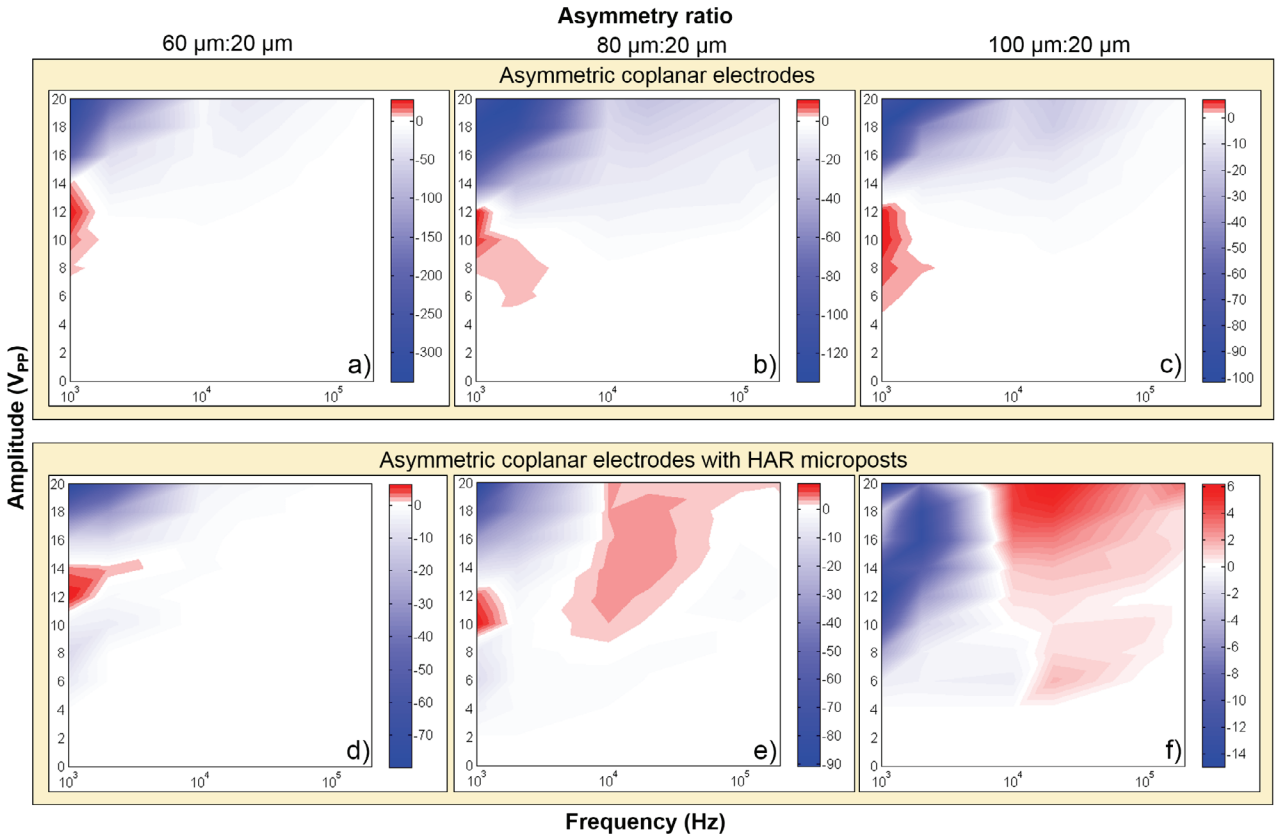

Figure 11. Color maps of measured fluid velocity for asymmetric-coplanar electrodes: (a)–(c) for devices (i), (ii) and (iii), respectively; and asymmetric-coplanar electrodes with HAR microposts: (d)–(f) for devices (iv), (v) and (vi), depending on applied AC magnitudes and frequencies. Red and blue colors indicate forward and reverse flow regimes, respectively; intensity of the hue indicates the relative magnitude of the flow velocity.

(i.e. developed on same electrode finger) collide with each other before completing a full vortex, thus propelling the fluid in the opposite direction. This suggests that micropost separation should be increased to allow complete vortex formation; however, the amount of microposts on the electrode would be reduced in consequence, considerably decreasing the electrode surface area in contact with the fluid for a constant microchannel width.

This effect would also explain the fluid direction switching from reverse to forward in the forward regime (from 4 to 14 V_{PP} and between 1 and 2 kHz, as shown in figures 11(d) and (e)), and the eventual fully reverse flow in both forward and reverse regimes at low frequencies (figure 11(f)). We have shown that the highest velocity for the tested planar devices is achieved by the lowest asymmetry ratio (i.e. 60 μm:20 μm) by achieving the largest horizontally-driven vortex formation. However, the short distance between adjacent microposts (~57 μm) and the large height (80 μm) allows vertically-driven vortices to propel fluid at low amplitudes due to the small vortex size required to drive the fluid in the reverse direction, since two facing electrode surfaces contribute to this task. Once the coplanar surfaces become dominant due to a higher horizontally-driven vortex size, the fluid switches to a forward propulsion and continues until reaching the reverse regime. This effect applies for all devices and, as the coplanar surfaces become less dominant with the increase on asymmetry ratio, the vertically-driven vortices become dominant until only reverse flow is achieved at low frequencies.

These results also suggest that HAR microposts can be used to produce fluid velocities of fairly similar magnitudes in forward and reverse directions, yielding symmetric flow by diminishing reverse flow and amplifying forward flow. For the case of the three asymmetry ratios characterized in this work, the ratio of maximum reverse regime velocity to the maximum forward regime velocity was reduced as the electrode asymmetry ratio increased: 12.55, 9.81, 2.41 for devices (iv), (v) and (vi), respectively, indicating that, as the electrode asymmetry ratio increases, forward and reverse flows become more symmetric, while a net fluid velocity decreases. This effect can be observed on figure 11(f), where red and blue hues have practically the same intensity in some points. This behavior is contrasted to that for coplanar electrodes without posts, where the reverse/forward fluid velocity ratio remained nearly constant.

4. Conclusions

In this work, we presented results of bidirectional fluid pumping with AC electroosmosis due to hydrodynamic channeling to control flow reversal in a microchannel using GC electrodes. From the three asymmetry ratios evaluated in this study, the smallest ratio (60 μm:20 μm) produced the highest fluid velocity, and velocity magnitude decreased as the electrode pairs' asymmetry increased. The use of HAR microposts leads to a reduction of the net fluid velocity for both, forward and reverse regimes; however, a trend for symmetric velocities was noticed as the electrode asymmetry ratio increased, suggesting that microposts can be used if nearly identical velocity profiles for forward and reverse fluid movements are desirable.

ACEO pumping represents a potential solution for the development of LoC-integrated fluid-driving mechanisms as it offers an easy on-chip integration, multiple fluid pumping chambers on a single microfluidic system, low power consumption, low fabrication costs, and bidirectional fluid pumping as demonstrated in the present work. Further advances of AC electroosmosis pumping can be gained by utilizing more conductive electrode materials as well as optimized electrode geometry.

Acknowledgments

This work was partly funded by the UC Mexus-CONACyT Collaborative Grant UCM-104728, the UC Mexus Small Grant UCM-104199, CONACyT CB2014-241458, and the CONACyT National Scholarship program #322105. Hyundoo Hwang acknowledges the support of the Bio and Medical Technology Development Program of the NRF funded by the Korean government, MSIT (2017M3A9E2062212/2017 M3A9E2062133). Lawrence Kulinsky gratefully acknowledges the support of the National Science Foundation (award CMMI-1661877).

Conflict of interest

The authors declare that they have no conflict of interest.

ORCID iDs

Sergio O Martinez-Chapa https://orcid.org/0000-0003-2689-1166

References

[1] Laser D J and Santiago J G 2004 A review of micropumps *J. Micromech. Microeng.* **14** R35–64
[2] Nabavi M 2009 Steady and unsteady flow analysis in microdiffusers and micropumps: a critical review *Microfluid. Nanofluid.* **7** 599–619
[3] Cheng Z, Wu X D, Cheng J and Liu P 2017 Microfluidic fluorescence-activated cell sorting (μFACS) chip with integrated piezoelectric actuators for low-cost mammalian cell enrichment *Microfluid. Nanofluid.* **21** 9
[4] Inman W, Domansky K, Serdy J, Owens B, Trumper D and Griffith L G 2007 Design, modeling and fabrication of a constant flow pneumatic micropump *J. Micromech. Microeng.* **17** 891–9
[5] Machauf A, Nemirovsky Y and Dinnar U 2005 A membrane micropump electrostatically actuated across the working fluid *J. Micromech. Microeng.* **15** 2309–16
[6] Jiao Z J, Nguyen N T, Huang X Y and Ang Y Z 2007 Reciprocating thermocapillary plug motion in an externally heated capillary *Microfluid. Nanofluid.* **3** 39–46
[7] Abe H, Imai Y, Tokunaga N, Yamashita Y and Sasaki Y 2015 Highly efficient electrohydrodynamic pumping: molecular

isomer effect of dielectric liquids, and surface states of electrodes *ACS Appl. Mater. interfaces* **7** 24492–500
[8] Gregory T S, Cheng R, Tang G Y, Mao L D and Tse Z T H 2016 The magnetohydrodynamic effect and its associated material designs for biomedical applications: a state-of-the-art review *Adv. Funct. Mater.* **26** 3942–52
[9] Islam N and Askari D 2013 Performance improvement of an AC electroosmotic micropump by hydrophobic surface modification *Microfluid. Nanofluid.* **14** 627–35
[10] Gao M and Gui L 2014 A handy liquid metal based electroosmotic flow pump *Lab Chip* **14** 1866–72
[11] Seyed-Yagoobi J 2005 Electrohydrodynamic pumping of dielectric liquids *J. Electrostat.* **63** 861–9
[12] Lemoff A V and Lee A P 2000 An AC magnetohydrodynamic micropump *Sensors Actuators* B **63** 178–85
[13] Mitchell P 2001 Microfluidics—downsizing large-scale biology *Nat. Biotechnol.* **19** 717–21
[14] Lee C-Y, Lee G-B, Lin J-L, Huang F-C and Liao C-S 2005 Integrated microfluidic systems for cell lysis, mixing/pumping and DNA amplification *J. Micromech. Microeng.* **15** 1215–23
[15] Perez-Gonzalez V H, Ho V, Vazquez-Pinon M, Martinez-Chapa S O and Kulinsky L 2015 A novel micro/nano fabrication process based on the combined use of dielectrophoresis, electroosmotic flow, and electrodeposition for surface patterning *J. Micromech. Microeng.* **25** 115007
[16] Cheng I F, Yang H L, Chung C C and Chang H C 2013 A rapid electrochemical biosensor based on an AC electrokinetics enhanced immuno-reaction *Analyst* **138** 4656–62
[17] Bown M R and Meinhart C D 2006 AC electroosmotic flow in a DNA concentrator *Microfluid. Nanofluid.* **2** 513–23
[18] Melvin E M, Moore B R, Gilchrist K H, Grego S and Velev O D 2011 On-chip collection of particles and cells by AC electroosmotic pumping and dielectrophoresis using asymmetric microelectrodes *Biomicrofluidics* **5** 034113
[19] Ramos A, Morgan H, Green N G and Castellanos A 1999 AC electric-field-induced fluid flow in microelectrodes *J. Colloid Interface Sci.* **217** 420–2
[20] Zengerle R, Ulrich J, Kluge S, Richter M and Richter A 1995 A bidirectional silicon micropump *Sensors Actuators* A **50** 81–6
[21] Choi W and Park J-K 2006 A bio-fluidic device for adaptive sample pretreatment and its application to measurements of *Escherichia coli* concentrations *Biotechnol. Bioproc.* E **11** 54–60
[22] Huang S B, Wu M H and Lee G B 2009 A tunable micro filter modulated by pneumatic pressure for cell separation *Sensors Actuators* B **142** 389–99
[23] Aeinehvand M M, Ibrahim F, Harun S W, Al-Faqheri W, Thio T H G, Kazemzadeh A and Madou M 2014 Latex micro-balloon pumping in centrifugal microfluidic platforms *Lab Chip* **14** 988–97
[24] Li C Y, Dong X L, Qin J H and Lin B C 2009 Rapid nanoliter DNA hybridization based on reciprocating flow on a compact disk microfluidic device *Anal. Chim. Acta* **640** 93–9
[25] Hosseini S, Aeinehvand M M, Uddin S M, Benzina A, Rothan H A, Yusof R, Koole L H, Madou M J, Djordjevic I and Ibrahim F 2015 Microsphere integrated microfluidic disk: synergy of two techniques for rapid and ultrasensitive dengue detection *Sci. Rep.* **5** 16485
[26] Choi S, Goryll M, Sin L Y M, Wong P K and Chae J 2011 Microfluidic-based biosensors toward point-of-care detection of nucleic acids and proteins *Microfluid. Nanofluid.* **10** 231–47
[27] Kim E S, Gustenhoven E, Mescher M J, Pararas E E L, Smith K A, Spencer A J, Tandon V, Borenstein J T and Fiering J 2014 A microfluidic reciprocating intracochlear drug delivery system with reservoir and active dose control *Lab Chip* **14** 710–21
[28] Mardegan A, Kamath R, Sharma S, Scopece P, Ugo P and Madou M 2013 Optimization of carbon electrodes derived from epoxy-based photoresist *J. Electrochem. Soc.* **160** B132–7
[29] Pramanick B, Vazquez-Pinon M, Torres-Castro A, Martinez-Chapa S O and Madou M 2018 Effect of pyrolysis process parameters on electrical, physical, chemical and electrochemical properties of SU-8-derived carbon structures fabricated using the C-MEMS process *Mater. Today-Proc.* **5** 9669–82
[30] Rouabah H A, Park B Y, Zaouk R B, Morgan H, Madou M J and Green N G 2011 Design and fabrication of an ac-electro-osmosis micropump with 3D high-aspect-ratio electrodes using only SU-8 *J. Micromech. Microeng.* **21** 035018
[31] Song Y, Agrawal R and Wang C L 2015 C-MEMS for biosensing applications *Proc. SPIE 9493 Energy Harvesting and Storage: Materials, Devices, and Applications VI* 949301
[32] Kim D, Pramanick B, Salazar A, Tcho I-W, Madou M J, Jung E S, Choi Y-K and Hwang H 2016 3D Carbon electrode based triboelectric nanogenerator *Adv. Mater. Technol.* 1600160
[33] Yang Y J, He L, Tang C J, Hu P, Hong X F, Yan M Y, Dong Y X, Tian X C, Wei Q L and Mai L Q 2016 Improved conductivity and capacitance of interdigital carbon microelectrodes through integration with carbon nanotubes for micro-supercapacitors *Nano Res.* **9** 2510–9
[34] Ramos A, Gonzalez A, Castellanos A, Green N G and Morgan H 2003 Pumping of liquids with ac voltages applied to asymmetric pairs of microelectrodes *Phys. Rev.* E **67** 056302
[35] Brown A B, Smith C G and Rennie A R 2001 Pumping of water with ac electric fields applied to asymmetric pairs of microelectrodes *Phys. Rev.* E **63** 016305
[36] Debesset S, Hayden C J, Dalton C, Eijkel J C T and Manz A 2004 An AC electroosmotic micropump for circular chromatographic applications *Lab Chip* **4** 396–400
[37] Amato L, Heiskanen A, Hansen R, Gammelgaard L, Rindzevicius T, Tenje M, Emneus J and Keller S S 2015 Dense high-aspect ratio 3D carbon pillars on interdigitated microelectrode arrays *Carbon* **94** 792–803
[38] Tuinstra F and Koenig J L 1970 Raman spectrum of graphite *J. Chem. Phys.* **53** 1126–30
[39] Maslova O A, Ammar M R, Guimbretiere G, Rouzaud J N and Simon P 2012 Determination of crystallite size in polished graphitized carbon by Raman spectroscopy *Phys. Rev.* B **86** 134205
[40] Gonzalez A, Ramos A, Green N G, Castellanos A and Morgan H 2000 Fluid flow induced by nonuniform ac electric fields in electrolytes on microelectrodes. II. A linear double-layer analysis *Phys. Rev.* E **61** 4019–28
[41] Ajdari A 2000 Pumping liquids using asymmetric electrode arrays *Phys. Rev.* E **61** R45–8
[42] Ren Y K, Liu W Y, Wang Z J and Tao Y 2018 Induced-charge electrokinetics in rotating electric fields: a linear asymptotic analysis *Phys. Fluids* **30** 062006